Journal of *Imaging*

MDPI

Review

Thermal Imaging of Electrochemical Power Systems: A Review

James B. Robinson †, Paul R. Shearing † and Daniel J. L. Brett *,†

Received: 1 October 2015; Accepted: 20 November 2015; Published: 6 January 2016
Academic Editor: Carosena Meola

Electrochemical Innovation Lab, Department of Chemical Engineering, UCL, London WC1E 7JE, UK; james.robinson.11@ucl.ac.uk (J.B.R.); p.shearing@ucl.ac.uk (P.R.S.)
* Correspondence: d.brett@ucl.ac.uk; Tel.: +44-020-7679-3310
† These authors contributed equally to this work.

Abstract: The performance and durability of electrochemical power systems are determined by a complex interdependency of many complex and interrelated factors, temperature and heat transfer being particularly important. This has led to an increasing interest in the use of thermal imaging to understand both the fundamental phenomena and effects of operation on the temperature distribution and dynamics in these systems. This review describes the application thermal imaging and related techniques to the study of electrochemical power systems with the primary focus on fuel cells and batteries. Potential opportunities and directions for future research are also highlighted, indicating the wide scope for further insights to be gleaned using infrared thermal imaging techniques.

Keywords: infrared imaging; thermal imaging; thermal management; electrochemical power systems; fuel cell; solid oxide fuel cell; PEM fuel cell; Li-ion battery; electrolysis; Li-S battery

1. Introduction

Electrochemical power systems are used in a wide range of sustainable power generation and storage applications due to the high electrical efficiencies and low carbon emissions which typify such devices. Broadly, these power systems can be divided into fuel cells and batteries; however, these assignments encompass a significantly larger subset of classifications governed by the material of construction, operating temperature and the fundamental mechanisms which generate electricity. Common to all electrochemical power devices is the fact that chemical energy is converted directly to electrical energy, negating the intermediate mechanical steps required by conventional combustion techniques. This direct conversion ensures that the efficiency of electrochemical power systems is not limited by the Carnot cycle [1] and also governs the mechanisms of energy loss within the cells. Rather than a combination of thermal, mechanical and acoustic energy, electrochemical power systems dissipate waste energy primarily via thermal mechanisms. This review will focus mainly on Li-ion batteries (LIB) and on polymer electrolyte membrane (PEMFC) and Solid Oxide Fuel Cells (SOFC); allowing the description of the most commonly studied electrochemical devices within two distinct temperature windows—temperatures below 120 °C for both LIB and PEMFC and those above 600 °C for SOFC. The reason for these temperature windows is different in all cases; for instance, the 600 °C limit is imposed due to the poor ionic conductivity of most oxide ion conducting electrolyte in SOFCs [2,3]; however, in the case of LIBs exceeding this limit can result in cell decomposition [4–7], which can in turn lead to catastrophic failure of the devices [8–10]. The importance of temperature for operational and safety reasons on both fuel cells and batteries can be seen in the varied and abundant literature produced to model the thermal characteristics and behaviour of these devices, in addition to an ever-increasing quantity of experimental reports. These models, which range from simple one-dimensional thermal models to highly complex three-dimensional coupled thermal and

electrochemical analyses, show that irrespective of device, non-uniform temperature distributions can be present during operation; often resulting in operational issues for the devices in question. In compiling this review, the authors will attempt to outline the key works describing the use of thermal imaging, whilst also outlining potential opportunities for further work in this area.

Li-ion batteries have had a transformative effect on portable electronics since they were first commercialised by Sony in 1991; however, these devices are being employed in increasingly compact and power intensive environments, including in powertrains for automotives [11–13]. Recent high profile incidents [14,15] and safety concerns have resulted in a wide array of safety componentry and other safeguards being built into battery packs and has led to significant research into improved cell designs. However, these additional components add to the economic cost of systems, whilst reducing both the volumetric and gravimetric power density. As such, recent attention has turned to improving thermal management of Li-ion systems [16]; by enhancing thermal homogeneity the volume and weight of battery packs can be improved, whilst also prolonging the life of devices.

Li-ion batteries are constructed from three distinct layers, a graphitic anode, an aqueous electrolyte and a Li-based cathode, which varies in the chemistry used to identify the cell type. During discharge, lithium in a metallic state in a graphitic anode oxidizes, and then the released Li+ ions move across to the cathode, where they are intercalated into a metal oxide-based cathode. The electrons go through the external circuit from anode to cathode. As such, the generation of heat in a battery is a complex sum of entropic and Ohmic contributions associated with the reactions and the flow of current within the cell [17,18]. These processes result in significant temperature variations within the cell and between internal and surface regions [19,20]. Despite this, the surface temperature of a battery can be related to the internal temperatures using a variety of techniques [21,22], and is of course vital in the thermal management of systems [23,24].

Polymer Electrolyte Membrane Fuel Cells (PEMFC) are a class of fuel cell which utilise an aqueous polymeric electrolyte to separate the electrodes. These devices are typically fuelled with hydrogen which is oxidized at the anode during operation using oxygen. This reaction results in the generation of water at the cathode (an exothermic process) which helps to maintain the ionic conductivity of the polymer membrane. The electronic current (generated at the anode) can produce non-uniform temperature distributions throughout the Membrane Electrode Assembly (MEA) through poor electrical contact, localised electrochemical reactions or hot spots associated with pin holes in the membrane electrolyte amongst other factors. A typical polymer electrolyte membrane fuel cell MEA is shown schematically in Figure 1.

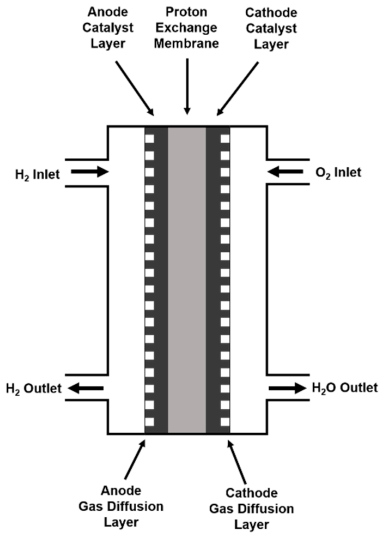

Figure 1. Typical structure of a Polymer Electrolyte Membrane Fuel Cell (PEMFC) showing the Membrane Electrode Assembly (MEA) and reactant and product stream flows.

As the membrane must be hydrated to operate effectively, PEMFCs have typically been limited to an operating temperature below 120 °C; however, this temperature restricts the choice of catalyst for cells, which is often platinum. In addition to increasing the cost of cells, the use of platinum also limits the level of impurities, including carbon monoxide and sulfur oxides, within the fuel which can be tolerated by PEMFCs. As such, a drive to increase the temperature has resulted in the development of high temperature membranes [25] and non-platinum metal catalysts [26]. With the developments in catalyst technology, the use of PEMFCs has steadily increased since the start of the 21st century, with a number of vehicles being produced using hybridised PEMFC technology. Portable devices have also been brought to market using so called "open-cathode" PEMFC which use atmospheric oxygen as the oxidant. In addition to localised electrochemical reactions, fuel cells are subject to a number of losses which result in heat generation. These losses, which arise due to deviations from the thermodynamic open circuit potential of the system, result from polarisations associated with the activation energy of the system along with Ohmic losses and mass transport losses. The magnitude of these combined polarisations is heavily dependent on the operation of the cell which in turn may lead to increased thermal heterogeneity. The generation of water within fuel cell systems also results in the formation of localised, internal heat sinks in PEMFC systems as water has a significantly higher thermal mass than the equivalent mass of H_2 and O_2 gas which results in a greater capacity to remove heat. In addition should the water condense the effect of latent heat on the temperature distribution must be considered. As such, temperature variations within these devices are a complex combination of chemical and physical contributions, which can vary with time, operating conditions and due to external factors.

Solid Oxide Fuel Cells (SOFCs) operate at high temperature due to the limits imposed by the ionic conductivity of the solid ceramic electrolyte layer utilised in the construction of the devices. The high operating temperature of SOFCs enables a much wider range of fuels to be used when compared to PEMFCs which has attracted interest in these devices for high power stationary operation. Heat recovery has also enabled SOFCs to be integrated into Combined Heat and Power (CHP) systems [27]. The increased operating temperature also enables non-precious metal catalysts to be used, with nickel commonly preferred. SOFCs are subject to the same polarisations as PEMFCs; however, a more significant cause of localised temperature variations is the internal reformation of methane when the cell is fuelled using hydrocarbons. Whilst this mode of operation has the advantage of being able to easily integrate with existing gas distribution infrastructure the reformation of methane occurs via interconnected and highly endothermic reactions (Equations (1)–(3)) which can generate severe thermal gradients on the surface of SOFCs [28,29].

$$CH_4 + H_2O \leftrightarrow 3H_2 + CO,\ \Delta H^{\circ}_{298} = 206\ \text{kJ}\cdot\text{mol}^{-1} \quad (1)$$

$$CH_4 + CO_2 \leftrightarrow 2H_2 + 2CO,\ \Delta H^{\circ}_{298} = 247\ \text{kJ}\cdot\text{mol}^{-1} \quad (2)$$

$$CO + H_2O \leftrightarrow H_2 + CO_2,\ \Delta H^{\circ}_{298} = 41\ \text{kJ}\cdot\text{mol}^{-1} \quad (3)$$

These gradients have been reported to result in significant stress distributions within SOFCs [30,31] and significantly increase the degradation of cells and contribute to the failure of stacks [32,33]. Indeed thermal gradients in excess of 10^4 $\text{K}\cdot\text{m}^{-1}$ have been reported under the conditions generated by methane fuelling [34] through finite element analysis, whilst experimental reports have also shown temperature gradients across the surface of small operational cells [35,36].

Irrespective of device, an effective thermal management strategy is paramount for both the safe and efficient operation of electrochemical power systems. As such, the use of infrared thermal imaging has garnered increasing interest, particularly with the decreased cost of infrared cameras. With this increased interest a diverse array of detector types, sensitivities and resolutions has been developed which has resulted in infrared cameras being developed which can be suited to a wide range of uses. For further information on fundamental aspects of thermal imaging the reader is referred to Vollmer and Mollmann [37] and Meola [38]. Broadly two types of cameras are suitable for infrared imaging of electrochemical devices—the medium and long wavelength cameras. The suitability of a specific

camera type depends on a large number of factors; however, is primarily governed by the operating temperature of the application in question. For this reason, specialized long-wavelength cameras (and indeed filtered CCD cameras) operating between 7 and 12 μm have typically been applied to high temperature SOFC research. The lower temperature devices have, in general, been examined using mid-wavelength cameras operating in a 2–5 μm bandwidth. Irrespective of device the quality of image obtained is heavily dependent upon the calibration of the camera performed prior to the experiments. Low emissivity, the presence of water and challenges in obtaining direct optical access to the device can result in misleading results. As such, it is imperative that the composition of the scene is considered before absolute temperatures are obtained. Indeed should the emissivity of the object being imaged be low, sources of radiation external to the scene may require consideration as a result of high reflectivity. In instances where changes to the device may occur—for instance the generation of water in PEM systems, the results must be analysed in such a way that these changes are accounted for; often through a time-dependent emissivity function.

The following sections will detail the use of thermal imaging under a number of scenarios: single frame thermal imaging to identify temperature distributions under a discrete condition, dynamic imaging showing temperature distributions which manifest temporally due range of operational and failure conditions and finally the use of thermal imaging in conjunction with additional techniques such as X-ray microtomography and Raman spectroscopy to enable thermal effects to be related to various structural or chemical changes.

2. Single Frame Imaging

Single frame thermal imaging has been widely used in order to obtain boundary conditions for models, or indeed, for model validation. However, single frames can also be used to describe the steady-state condition of devices with high accuracy. This mode of operation can also be used as a diagnostic—identifying areas of high or low electrochemical activity, thus elucidating vital information in the design and optimisation of systems. Air breathing PEMFCs were examined by Obeisun *et al.* [39] who looked at the temperature distributions, shown in Figure 2, associated with the passive fuelling strategy employed by these devices. An increased operating current was seen to result in increased surface temperatures, with inhomogeneous distributions being imposed on the device by the housing in which it was contained. The effect of clamping pressure was also observed to have an impact on the temperature distribution; with lower clamping pressures in the center of the cell resulting in a lower temperature, this was attributed to poor electrical contact.

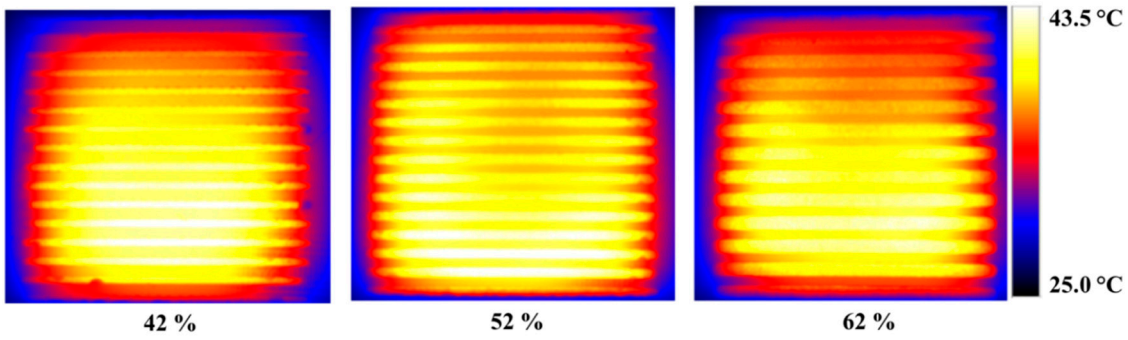

Figure 2. Images showing the effect of the opening ratio (*i.e.*, the area of electrode exposed to the atmosphere) of an air breathing PEMFC obtained by Obeisun *et al.* [39]. Heterogeneous temperature distribution is clearly visible on the cell due to non-uniform clamping forces and the flow configuration in the system. Water formation can be seen at the edges of the cell at the 42% opening ratio. Reproduced with permission from [39].

As a result of this finding it was suggested that by increasing the opening ratio of the cell (in doing so enabling more oxidant to reach the cell) the temperature at the centre of the cell may in fact decrease. Further work suggested that circular openings improved the electrical contact of the cell, enabling a larger opening ratio in the current collector, whilst maintaining sufficient electrical contact with the cell [40].

Martins *et al.* have validated a one-dimensional PEMFC model using thermal imaging [41]. Once more a non-uniform temperature distribution was observed; however, in this instance measurements were taken from the plastic fuel cell housing. Temperature variations of 6.5 °C (approximately 20% of the maximum absolute temperature) were observed at low operating currents (1.5 A). These variations, which were seen despite the additional thermal mass added by the plastic housing, were observed to be in agreement with the model that the authors produced, which accounted for temperature variations along the flow channel. A similar approach was taken by Matian *et al.* who used thermal images to validate a heat transfer model for PEMFCs [42]. To conduct this work the surface of a multi-cell stack was coated with a matte paint to achieve a uniform emissivity across the various layers which comprise the system. The temperatures obtained via infrared imaging were seen to be within 5% of the predicted values, with variations associated with the gas flow directions described. Additionally it was observed that the absolute temperature was higher on the cathode (air side) of the cell. The temperatures at the respective gas entry and exit points was seen to vary significantly, with the surface temperature decreasing by 33 °C between the air inlet and outlet. The temperature between the hydrogen inlet and outlet was also seen to increase by 8 °C. The work, highlighted in Figure 3, was subsequently expanded to include multiple cells with good agreement between the experimental results and the model observed once again.

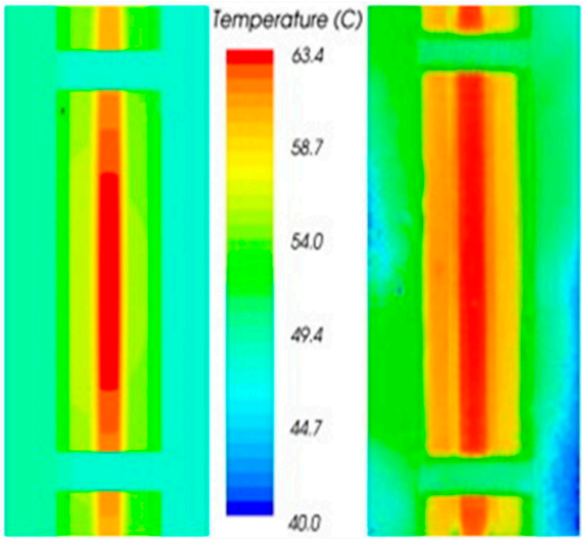

Figure 3. Comparison of the temperature distribution of a two cell PEMFC system obtained using finite element analysis (**left**) and thermal imaging (**right**) reported by Matian *et al.* [42]. Good agreement is seen between the computational and experimental results, highlighting the impact of thermal imaging as a tool for model validation. Reprinted from [42] with permission from Elsevier.

The flow direction of reactants was also seen to have an impact on a PEM device operated in electrolysis mode to generate H_2 gas through the electrochemical splitting of water by Dedigama *et al.* [43]. The authors showed a linear relationship between the operating current density and temperature of the electrolysing device at a number of operating current densities. In this instance the device was not painted; however, emissivity corrections were applied during the analysis of the results. Furthermore, the rate of heat loss was linked to the efficiency of the system which may be used to find an ideal operating point for PEM electrolysers.

In order to gain optical access to the surface of fuel cell electrodes modification of the system is often required, as demonstrated by Hakenjos and Hebling [44] who used a ZnSe window to observed the temperature at a PEMFC cathode. The interaction between cooling gas streams and heat generating electrochemical reactions was observed, with a complex temperature distribution visible through the infrared measurements. Shimoi *et al.* also used a window to examine the temperature distribution along flow channels in PEMFCs [45] this study highlighted water droplet formation as a major challenge to obtaining accurate thermal images of the cathode as evident in Figure 4. Once again hot-spots were observed at the electrode surface and a dependence between the operating condition and temperature was seen.

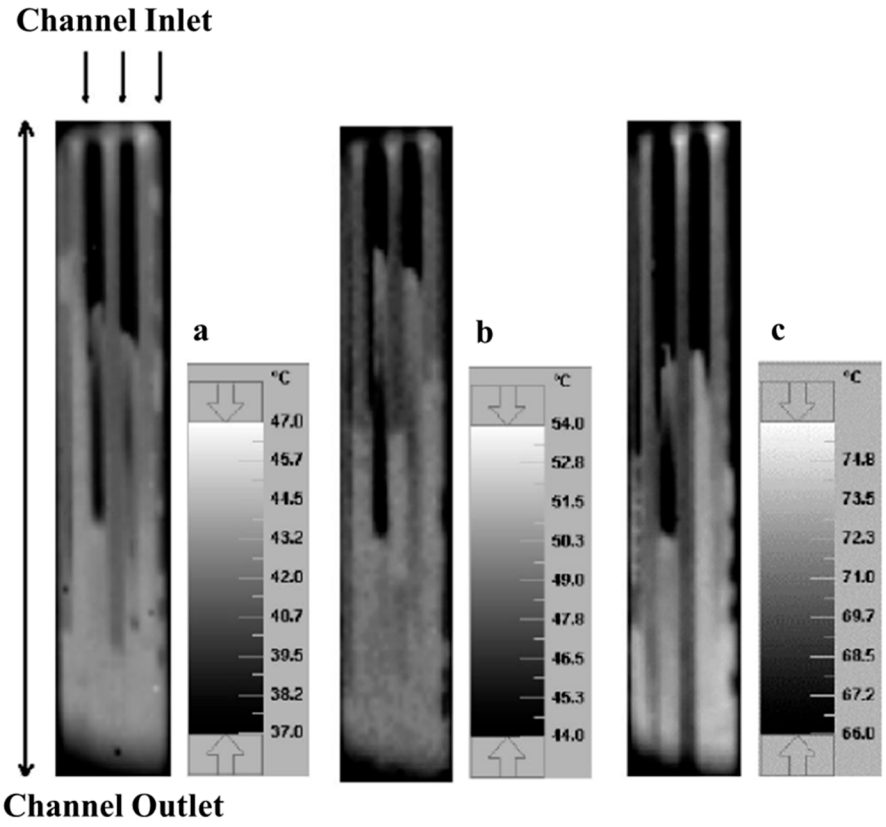

Figure 4. The temperature distribution of a PEMFC cathode observed through a sapphire window as reported by Shimoi *et al.* [45] at three operating current densities: (**a**) 345 mA· cm^{-2}; (**b**) 556 mA· cm^{-2} and (**c**) 992 mA· cm^{-2}. Water formation and adherence to the window is clearly visible which masks the lower portion of the electrode in all measurements. Reprinted from [45] with permission from ASME.

Water formation also inhibited the imaging of the cathode temperature distribution in a study reported by Guo *et al.* [46]. Despite this the authors were able to successfully image the anode (fuel side) of a PEMFC using a BaF_2 window. As this side of the fuel cell does not produce water, condensation on the window was not observed. This study showed increased temperature activity at both edges of the system which utilised an interdigitated flow field configuration as seen in Figure 5. This was attributed to increased gas pressure in these areas, which in turn, increased the rate of electrochemical activity. A cooler region was observed in the middle of the cell which was suggested to be as a result of lower pressure due to the flow conditions. The effect of operating current densities was examined with small non-uniform temperature distributions being visible at 0.424 A· cm^{-2}; these heterogeneities were seen to increase with increasing current densities.

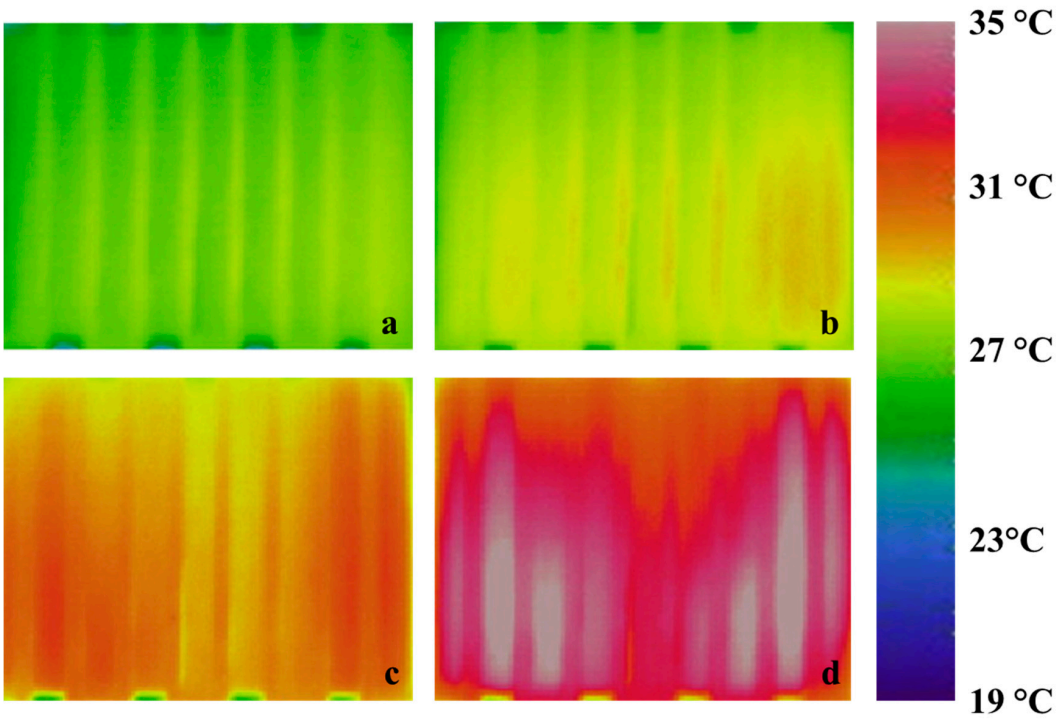

Figure 5. PEMFC anode temperature distribution measured through a BaF_2 window by Guo *et al.* [46] at current densities of: (**a**) 424 mA·cm^{-2}; (**b**) 742 mA·cm^{-2}; (**c**) 1061 mA·cm^{-2}; (**d**) 1379 mA·cm^{-2}. The effect of flow direction is seen most clearly in image (d) via the cold spot located in the middle of the cell. Reprinted from [46] with permission from Elsevier.

Rather than inhibit the measurement as discussed previously, Daino *et al.* [47] used infrared imaging to visualise water formation through the MEA of a PEMFC. In addition to obtaining thermal information pertaining to the through-plane temperature distribution, the authors utilised the highly emissive nature of water droplets to identify the respective phases of water at the anode and cathode. It was observed that liquid water was present at the cathode, whereas water transport primarily occurs in the vapour phase at the anode. This work highlighted potential uses for thermal imaging as a visualisation tool to identify areas and artefacts in systems which have to date been considered inhibitory to accurate thermal measurement.

Models for Li-ion cells have also been validated using thermal imaging. Kim *et al.* has reported the validation of thermal models using infrared imaging [48,49], shown in Figure 6; however, these studies only compared the model to a single discharge rate of 5 C (equivalent to 130 A), with the validation images given after a discharge time of 10.8 min showing the behaviour of the battery at a very low state of charge. Similar work was performed by Wang *et al.* [50] who performed finite element analysis to examine the transient response of the temperature distribution on the surface of a planar cell. This model was validated using single frame thermal images taken at 5 min intervals, which showed the temperatures at the current collecting tabs were higher than the average cell temperature.

The impact of cell design was studied by Waldmann *et al.* who investigated the thermal performance of six different cell designs [51]. In conducting this work the authors utilised thermal imaging on two of the designs, showing the deviations in surface temperatures which occur in planar and cylindrical cell designs. The thermographic results show that temperature distributions are significantly larger in the planar cells studied with variations approaching 20% observed. Work conducted at the National Renewable Energy Laboratory, primarily by Peseran and Keyser, have demonstrated the applicability of thermal imaging to investigate the thermal performance and characteristics of batteries which can be employed in both electric and hybrid vehicles. This work indicated an axial temperature distribution across the system, with large thermal gradients visible

at high discharge rates in a six cell system [52]. Further studies have shown a relatively uniform surface temperature distribution in a three cell system when cooling was present; however, mild heterogeneities were visible when the cooling was removed [53]. The research was then expanded to aid model development and battery design by Bharathan *et al.* [54] who charted the development of battery stacking technology by comparing the temperature distribution on two generations of power systems using similar cells, with a new method showing significantly more homogeneous temperature distribution and a lower overall operating temperature for the same discharge rate.

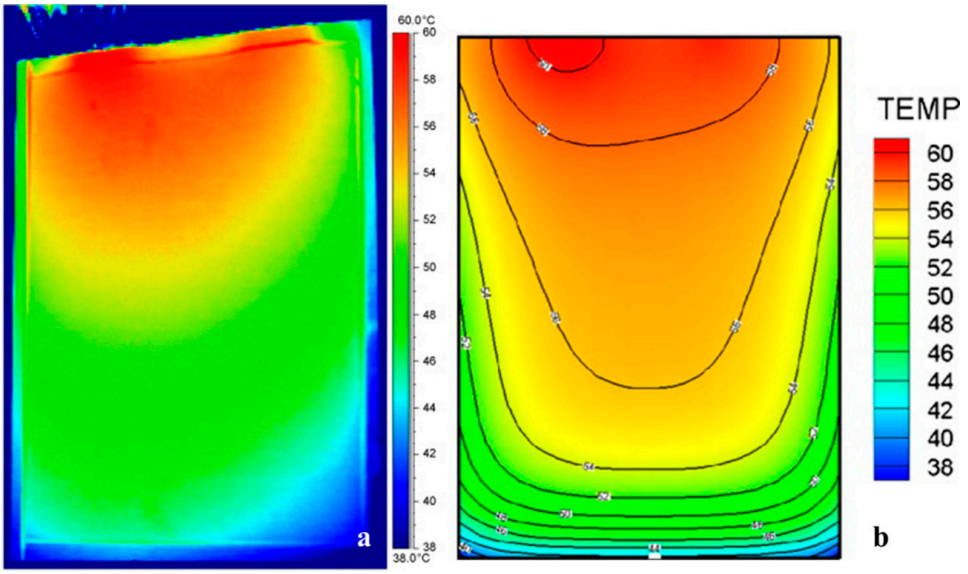

Figure 6. Validation of finite element analysis developed by Kim *et al.* [48] to investigate the surface temperature of Li-ion batteries. Good agreement between the experimental results (**a**) and computational results (**b**) are observed for this time point at a discharge rate of 5 C. Reprinted from [48] with permission from Elsevier.

3. Dynamic Thermal Imaging

The use of dynamic thermal imaging has revealed the thermal effects of operational transients and failures of electrochemical devices. By examining these effects (and considering the entire system) control strategies can be altered to maximise the performance of both fuel cells and batteries. Noorkami *et al.* [55] used thermal imaging to validate a stochastic model aimed at incorporating temperature uncertainty into the operation of PEMFCs. This work involved the recording of thermal data at various points along the polarisation curve of an air cooled, open-cathode commercial PEMFC. Once statistically relevant samples of data were obtained, distribution functions were generated and used to generate polarisation curves which included the uncertainty associated with the temperature measurement. The model revealed that rather than the widely reported polarisation curve, a polarisation "band" results, which increases in width with increasing current. Additionally, it was observed that the fuel cell tended to operate towards a lower voltage, indicating that PEMFCs err towards poorer perceived performance due to the natural variation in temperature within a given system.

Meyer *et al.* has used thermal imaging to investigate the performance of commercial open-cathode PEMFCs under a range of conditions as seen in Figure 7. Dead-ended operation of the system was examined, showing a larger temperature rise with time during dead-ended operation than observed when the system was operated under through-flow conditions [56]. This behaviour was attributed to variations in the humidity within the system during operation, resulting in an increased current flow, and consequently an increased Joule heating effect.

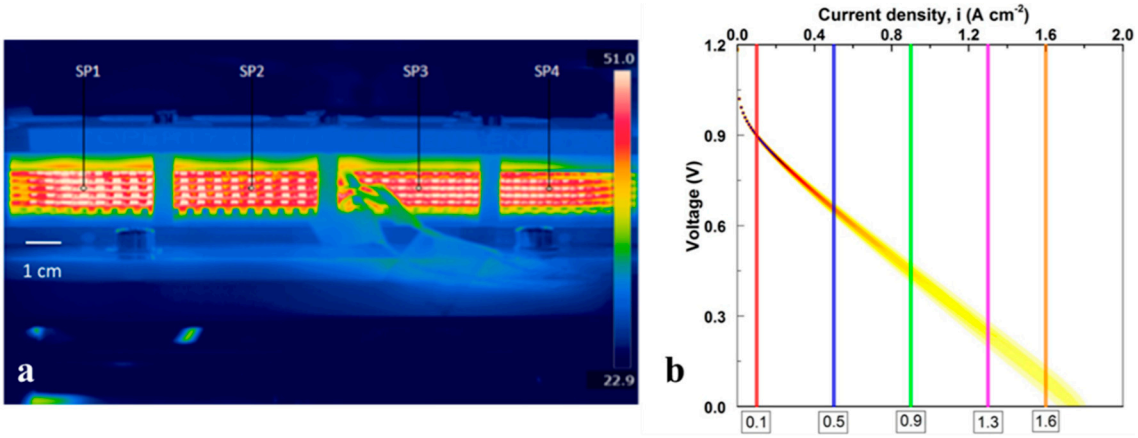

Figure 7. Results obtained by Noorkami *et al.* [55] highlighting the potential use for thermal imaging as a tool to inform models. Shown is: (**a**) a snapshot from images used to obtain statistically relevant temperature distributions from a commercial PEMFC stack which were later used to perform sensitivity analysis on the fuel cell polarisation curve; (**b**) which shows the importance of considering a polarisation "area" or "band" when operating a fuel cell system. Reproduced with permission from [55].

A novel application of lock-in thermography has been employed by Robinson *et al.* [57] to identify defects within Li-ion pouch cells. This technique uses an active sinusoidal stimulus (e.g., heat, light, acoustic) to increase the sensitivity of the detector in obtaining a frequency dependent amplitude image, whilst also enabling the acquisition of a phase image. Traditionally this technique has used a heat lamp as the stimulus to identify sub-surface defects in operational components. The work by Robinson *et al.* used the charge/discharge current of a Li-ion cell as stimulus, as illustrated in Figure 8.

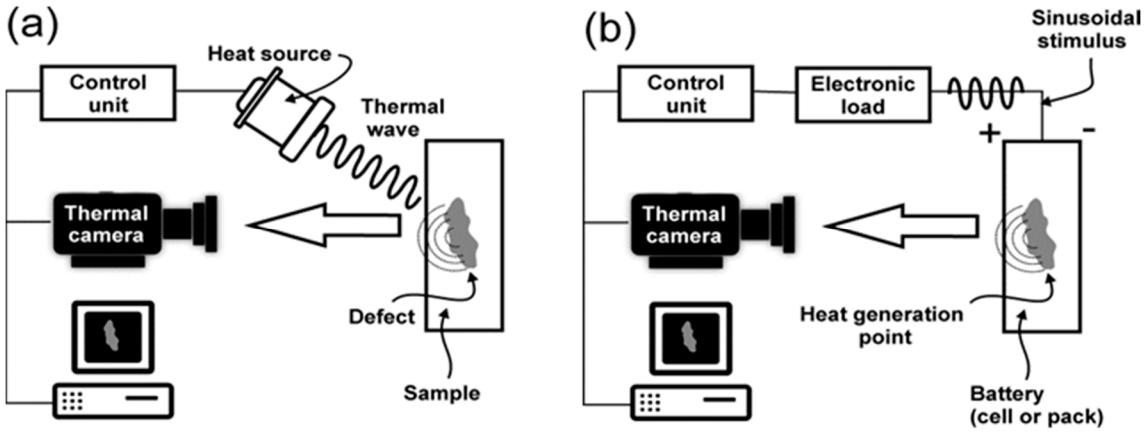

Figure 8. Overview of lock-in thermography process highlighting (**a**) the traditional use of a heat lamp to detect subsurface defects and (**b**) the modified use of the direct electrical current emplyed by Robinson *et al.* [57].

Work conducted using this novel experimental configuration showed that lock-in thermography can be used to identify internal structural deformation, as seen in Figure 9. The results show areas of increased electro-thermal impedance associated with areas of impaired heat transfer; in this instance it is associated with sub-surface gas pockets. It was suggested that this technique could have a significant impact on the study of Li-ion systems by enabling non-destructive identification of defects within cells *in operando*.

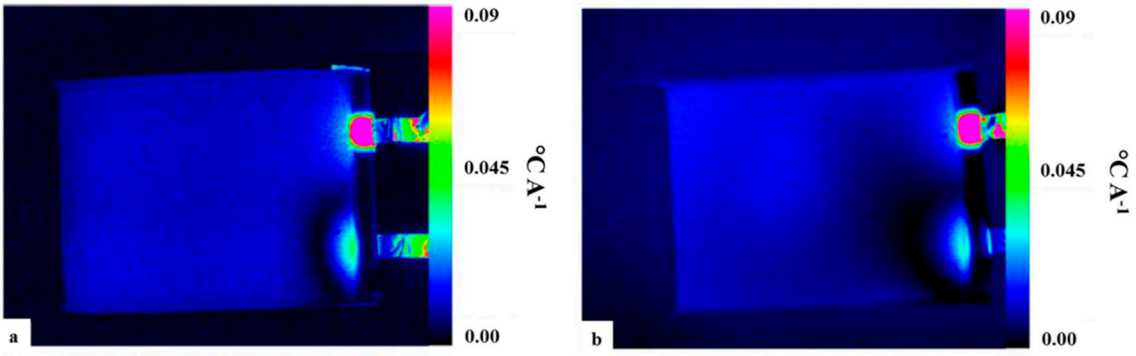

Figure 9. Lock-in thermography images reported by Robinson *et al.* [57] showing the amplitude images of a fresh (**a**) and aged (**b**) cell investigated at 0.1 Hz. The effect of gas formation is clearly visible in the aged cell which shows a lower response throughout the bulk of the cell. Reproduced with permission from [57].

A similar technique was used by Engebretsen *et al.* [58] who combined lock-in thermography with a technique known as electrothermal impedance spectroscopy to investigate temperature distributions within an open-cathode PEMFC highlighting the potential for lock-in thermography as a tool in examining fuel cell systems.

Dynamic imaging of SOFCs was conducted by Pomfret *et al.* [59]; this work used low molecular weight alcohols (MeOH, EtOH) to observed the cooling effect of carbon formation as shown in Figure 10. It was observed that operating both using methanol and lower operating temperatures (below 750 °C) resulted in increased carbon formation; however, above this temperature limited carbon formation was reported. Operation using ethanol was seen to result in significant carbon formation at all temperatures. As previously discussed, the operation of SOFCs using hydrocarbons is associated with significant endothermic reactions and associated temperature gradients; this operation mechanism may also lead to the formation of carbon on the surface of the devices. These thermal gradients were observed *in operando*, while areas which were later revealed to be significantly damaged were also visible using thermal imaging. The highest cooling effect was observed under ethanol fuelling at an intermediate operational temperature of 750 °C; this result was ascribed to incomplete pyrolysis of the ethanol reactant. This work built upon foundations laid by the same author which detailed the effect of changing reactant flow from hydrogen to propane [60]; and was subsequently expanded to investigate the effect of humidification on ethanol in subsequent articles [61,62]. Once more, thermal gradients associated with fuel cracking were observed; however, it was reported that increasing the humidity of the inlet ethanol feed reduced the cooling effect. Despite this, areas of damage to the cell were reported for operation at 750 °C using wet ethanol; in contrast, operation of the cell under similar conditions using dry ethanol did not cause damage. Further work comparing the effects whilst operating under methanol and methane flows showed similar results; with cooling effects due to the cracking of hydrocarbon reactants reported across the surface of the SOFC anode [63].

Reports of thermal imaging of large SOFCs under hydrogen operation are limited; however, Brett *et al.* [64] used infrared imaging to investigate the effect of cell polarization on a small pellet cell, seen in Figure 11. In order to access the cell, only the cathode was imaged with temperature rises of approximately 2.5 °C at a current density of 270 mA·cm^{-2}. It was observed that the temperature rise associated with cell polarization was higher at lower operating temperatures and it was also reported that by neglecting the increase in temperature, models risked underestimating the power available from the cell, particularly at high current densities. This prediction was enabled by calculating a total heat transfer coefficient for the cell from the thermal images obtained, highlighting the suitability of thermal imaging when validating models. Further work (also shown in Figure 11) conducted by Schöttl and Brett [65] examined the effect of thermal shock on SOFCs, with relatively low flows of

cooling gas (N_2) being sufficient to result in substantial temperature gradients (up to 10 °C· mm^{-1}) in the surface temperature of the cell—potentially inducing significant stress gradients.

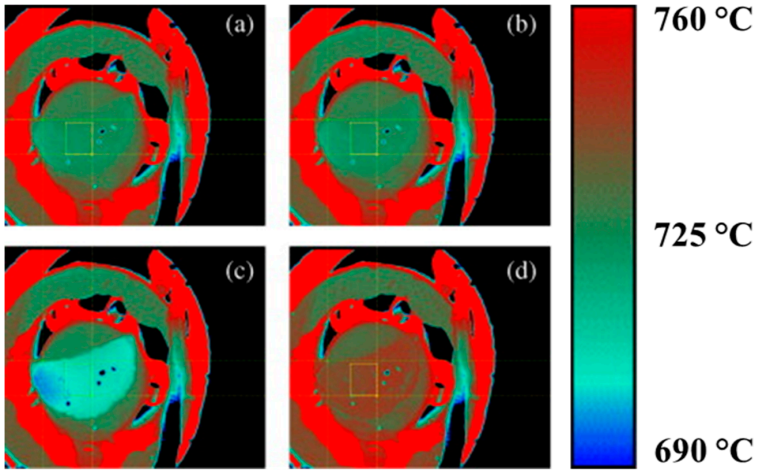

Figure 10. Near infrared thermal images of an 25 mm diameter SOFC under Ar (**a**) with the maximum temperature changes shown for changes in flow to (**b**) a H_2/Ar mixture, (**c**) propane/Ar mixture and (**d**) air as reported by Pomfret *et al.* [59]. Reproduced with permission from ACS from [59].

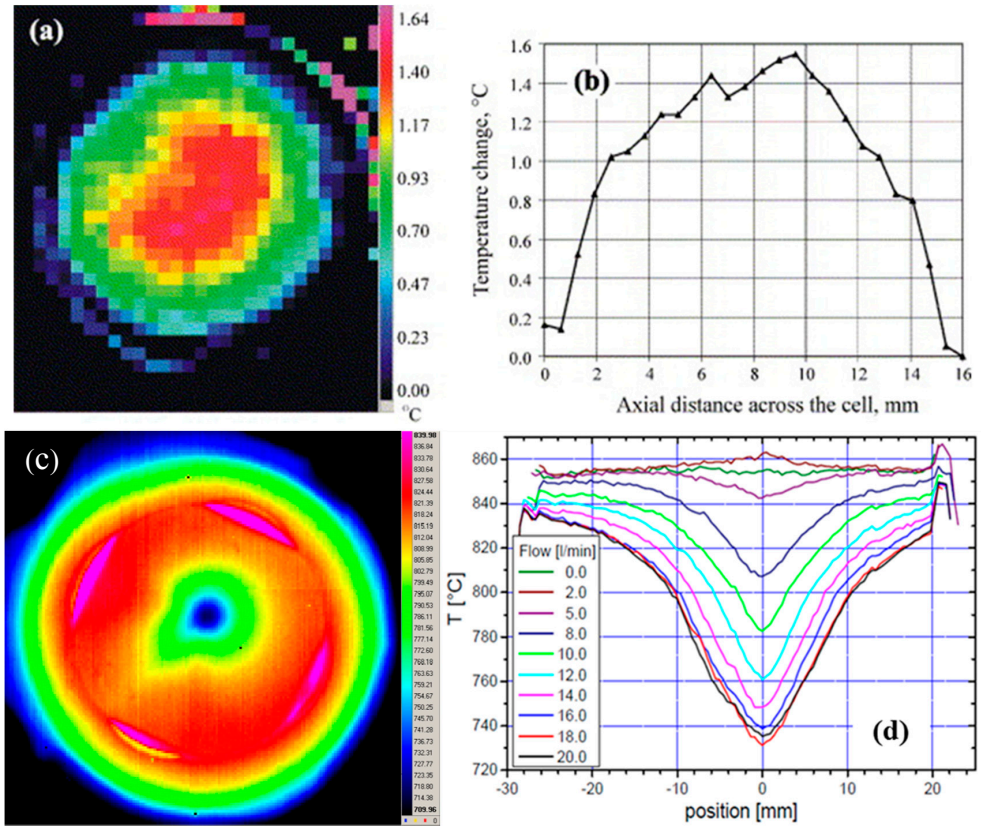

Figure 11. Infrared image (**a**) and temperature distribution (**b**) of a pellet SOFC [64]. Also shown is the effect of introducing a cool N_2 stream to the surface of a SOFC cell (**c**) which is seen to generate large thermal gradients (**d**), as reported by Schöttl and Brett [65]. Reproduced from [64] with permission from Elsevier.

SOFCs were examined in electrolysis mode by Cumming *et al.* [66,67] who showed that temperature rises were similar irrespective of the location, or absolute temperature of the cell. It was suggested that this observation (which contradicts that reported by Brett *et al.* [64] for operation in fuel cell mode) was as a result of the decreased electrolyte thickness. It was further reported that the concentration of hydrogen has an impact upon the rate at which the temperature rises; however, the ultimate temperature remains the same under both conditions. An observable change between endothermic and exothermic conditions was observed as the SOFC was reduced in voltage from 1.5-0.85 V, the extent of which was dependent upon the fuel-side reactant. Operation under steam rich conditions was seen to have a significantly smaller endothermic effect than under CO_2 rich conditions, with the opposite occurring during the exothermic portion of the voltage sweep; while co-electrolysis was seen to result in a temperature difference which lay in between the two extreme conditions examined.

The failure of Li-S batteries was investigated by Hunt *et al.* who performed the industrially standard nail penetration test on such cells [68]. In doing so the effect of this critical safety test on the surface temperature distribution on the cells was examined. This test (shown in Figure 12) is used to evaluate the safety of battery systems to penetration by metallic objects with the associated short circuiting has been observed to cause substantial temperature rises in traditional Li-ion cells [69,70].

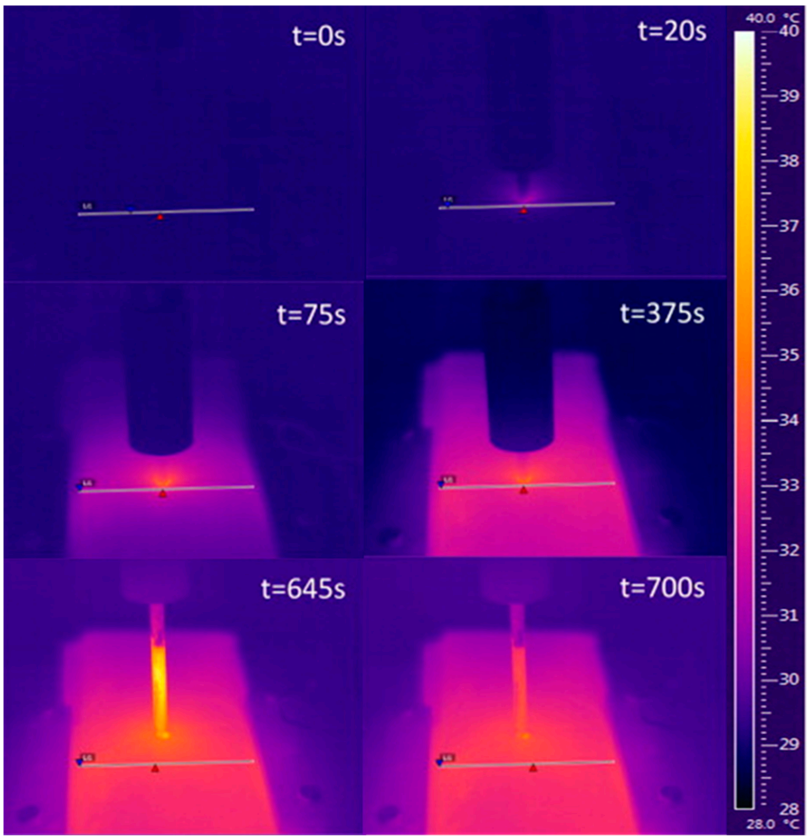

Figure 12. Dynamic thermal imaging charting the temperature change associate with a nail penetration test conducted on a Li-S cell of dimensions 180 mm × 75 mm × 8 mm by Hunt *et al.* [68]. Reproduced from [68] with permission from Elsevier

The work performed by Hunt *et al.* suggested that the Li-S chemistry which replaces the traditional graphite with sulphur in the anode are more stable to external short circuiting with a maximum temperature rise of 10 °C observed. Finite element analysis of Li-ion systems has also been validated using continuous thermal imaging. Kim *et al.* has shown excellent agreement between a

two-dimensional model during both charge and discharge under constant power operation [71]. This work was expanded to a three dimensional model which also considered external electrical contacts by Yi *et al.* [72] shown in Figure 13.

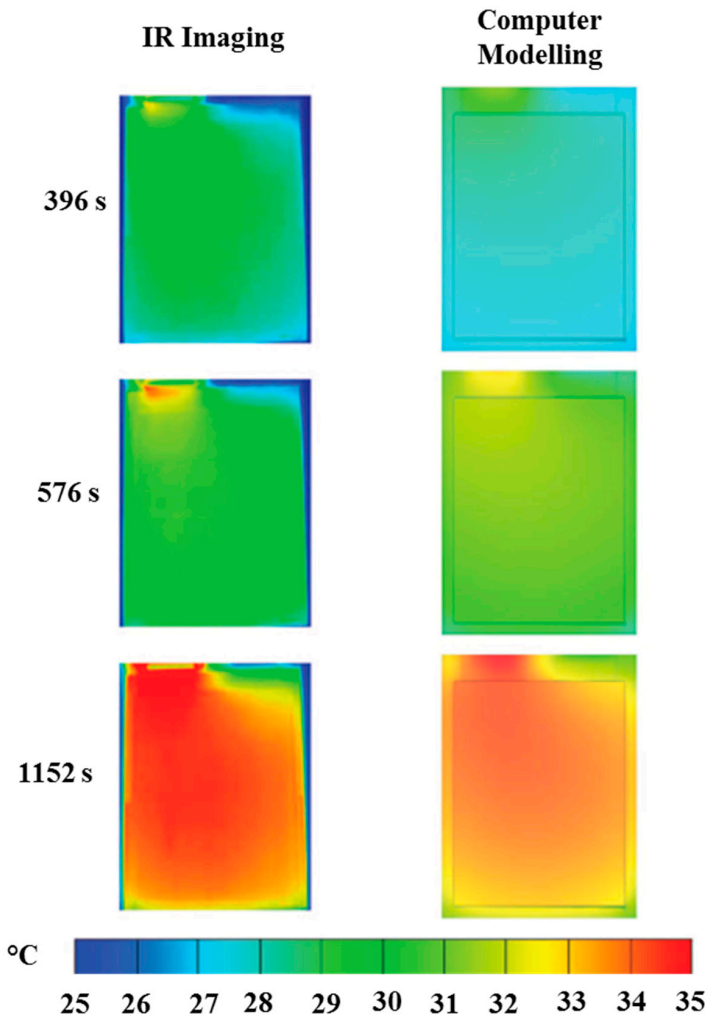

Figure 13. Comparison of thermal imaging and finite element analysis conducted by Yi *et al.* [72] showing improved agreement with increasing time at a discharge rate of 3C (equivalent to 43.8 A discharge). Note the effect of the electrical contacts (upper left) on the temperature distribution of the cell. The dimensions of the active cell examined are 194 mm × 147 mm × 5.4 mm respectively. Reproduced by permission of The Electrochemical Society.

In both instances, non-uniform temperature distributions were observed, with the extent of the inhomogeneity increasing with increasing current. However, including electrical contacts was seen to significantly exacerbate the complexity of the thermal distribution throughout the cell. Temporal variations in the level of agreement were observed in the model produced by Yi *et al.* [72] with the model being most representative at longer time intervals. Despite this, the model enabled the approximation of better temperature dynamics to be examined in great detail with relatively high precision; demonstrating the efficacy of thermal imaging as a tool for the validation of temporally dependent models.

A continuous temperature monitoring system incorporating thermal imaging which interfaces with LabVIEW has been reported by Qin *et al.* [50]. This has potential not only for steady state and transient monitoring but also in Quality Control (QC) processes. A QC methodology has also been demonstrated by Duan *et al.* to identify defective batteries using a high current charging process [73].

This work showed that defective cells showed both higher and faster surface temperature rises when compared to pristine cells. As the cost of thermal imaging devices continues to decrease, it is possible that these methodologies could be employed as a low cost automated screening process to monitor cells post production. Similar techniques may also be employed upon high risk power systems in vehicles and aerospace applications as a diagnostic to prevent catastrophic cell failure.

4. Correlative Metrology Employing Thermal Imaging

The use of a correlative metrological approach enables thermal imaging to be complemented by techniques which enable the systems examined to be understood in substantially more depth than otherwise. In performing a combined experiment, the dynamics of devices can be examined both *in situ* and *in operando*. There is no requirement, however, for sequential experimentation to identify causal mechanisms associated with the structure of devices. Robinson *et al.* have combined *ex situ* X-ray microtomography with thermal imaging and electrochemical impedance spectroscopy to identify the cause of non-uniform temperature distributions on the surface of cylindrical Li-ion cells [74], as displayed in Figure 14. This work showed the presence of metallic safety componentry located at the positive terminal contributed significantly to the heterogeneous thermal distributions at discharge rates within the manufacturer's specified operating window for the cell. Low clamping force, which results in poor electrical contact, was also identified as a potential cause of Joule heating at the negative terminal. Additionally, it was seen that a safety component known as a Positive Temperature Coefficient (PTC), which is used to prevent excessive discharge rates, was not activated up to an ambient temperature of 60 °C.

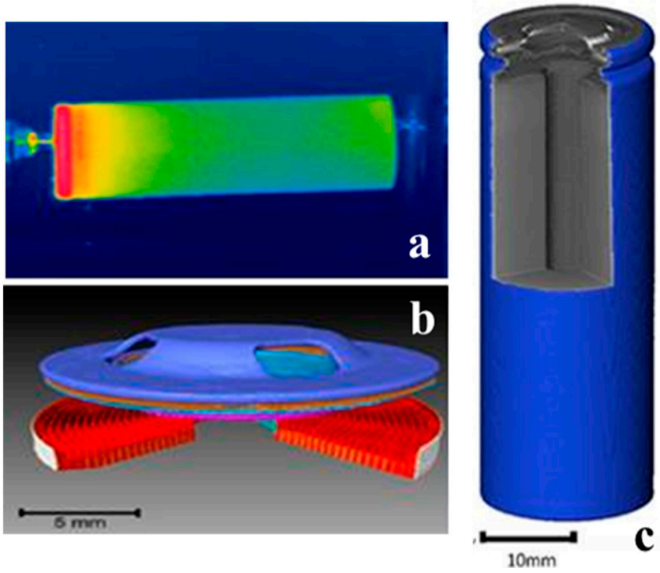

Figure 14. Representation of the correlative metrological approach employed by Robinson *et al.* [74] which ascribed the non-uniform temperature distributions (**a**) observed in 18,650 Li-ion cells under discharge to the presence of safety mechanisms within the cell housing (**b**). Also shown (**c**) is the reconstructed bulk of the battery which was investigated to ensure the heating was not caused by internal defects. Reproduced from [74] with permission from Elsevier.

Synchrotron radiation was employed by Finegan *et al.* to investigate thermal runaway in Li-ion cells [75]. This condition, which causes catastrophic failure of the cells, was examined *in operando* through a series of radiographic and tomographic measurements highlighting its devastating impact upon the internal structure of the cells highlighted in Figure 15. Infrared imaging was used to measure the surface temperature of the cells while it was subjected to thermal abuse designed to simulate conditions which would be experienced in the event of a fire. It was observed that thermal runaway

occurred when the surface temperature of the cell was within the region 230–260 °C. Hotspots were observed appearing on the surface of the cell using infrared imaging which is indicative of internal short circuits during the experiment. The Joule-Thompson effect was also observed through thermal imaging on the opening of the internal pressure relief valve. Transient thermal gradients in excess of 700 °C were reported across the 65 mm diameter cell with the internal temperature of the cell reaching in excess of 1085 °C as evident copper globules formed by the melting of internal current collector material.

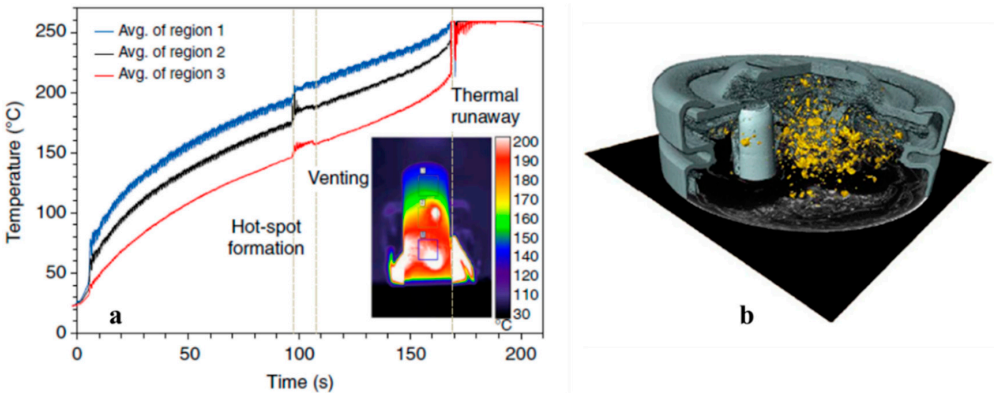

Figure 15. Temperature measurements obtained by Finegan *et al.* [75] showing: (**a**) the onset of thermal runaway and (**b**) *post mortem* tomographic reconstructions of the top of the cell after failure. Copper globules formed during the cell failure are shown in gold and indicate a temperature of 1085 °C within the cell during the failure process. Reproduced under Creative Commons CC license from [75].

Synchrotron radiation was also employed by Robinson *et al.* to investigate the effect of thermal gradients on stress distributions within the Ni-YSZ anodes employed in SOFCs [76] This work, which involved the construction of a special high temperature furnace compatible with the synchrotron beam line apparatus [77] utilised a fixed camera location in order to relate the one dimensional thermal gradients (shown in Figure 16) generated to the location of the diffraction measurements across the cell sample. It was observed across a range of temperatures that thermal gradients induce non-uniform stress distributions within the cell which exceeded those expected by up to 16%. This work informed finite element analysis, which incorporated the measured temperature field into the a computational models using COMSOL Multiphysics [78].

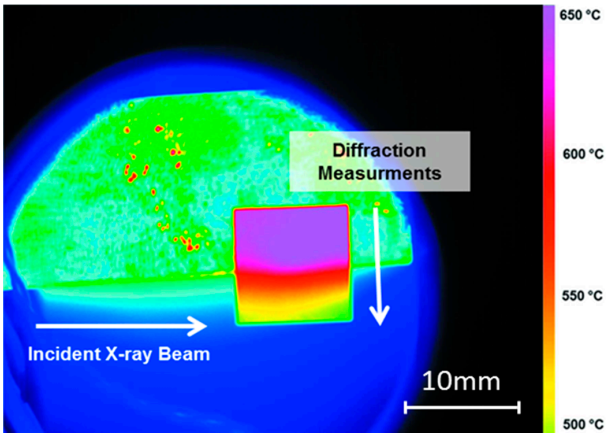

Figure 16. Thermal image obtained by Robinson *et al.* from a combined X-ray diffraction and thermal imaging study to investigate the effect of temperature gradients on the stress within Ni-YSZ composite ceramic structures used as SOFC anodes [76–78] .

The use of hydrocarbon fuels on the surface temperature of operational SOFCs was investigated by Kirtley *et al.* who combined thermal imaging with Raman spectroscopy and Fourier-transform infrared emission spectroscopy to give a holistic view of the processes occurring at the anode. Effects induced by methane were investigated and compared to those observed using biogas [79] The combination of these techniques enabled the reforming process to be examined in substantially more detail than was previously possible, with the study observing that both gaseous carbon emissions and solid phase carbon deposits were reduced when operating in biogas. As carbon deposition has widely been reported to significantly impair and degrade the performance of SOFCs, this finding highlights the potential use of SOFCs in a more sustainable manner. This work expanded upon initial research conducted by Eigenbrodt *et al.* to investigate [80] who once more combined thermal imaging with Raman spectroscopy to identify the type of carbon formed under both methane and methanol fuel flows. The inference of reactant cracking obtained using thermal imaging by the presence of large cooling effects was validated through concurrent Raman spectroscopy.

These synchronous studies highlight the benefit of a correlative approach when using thermal imaging—enabling processes to be identified in depth, which in turn results in an improved understanding of the mechanisms observed.

5. Conclusions

This review article has highlighted a number of key studies pertaining to thermal imaging of electrochemical devices. This area, while nascent, is rapidly expanding, as evident by the increasing quantity of articles utilising thermal imaging techniques to gain insights for both operational and modelling purposes. It is clear that thermal imaging can be used in both a "passive", single frame mode; however, the most significant insights can be gleaned in examining the transient operation of devices.

To date, the use of transient imaging to validate models has been limited; as such, an opportunity presents itself to produce rigorous and fully validated models for both steady and dynamic conditions. These models would provide the most accurate representation of electrochemical systems to date and simplify the design and operation of systems. In addition, the use of thermal techniques such as lock-in thermography and electro-thermal impedance, has received very little attention. These advanced thermal imaging techniques enable extremely small variations in temperature to be detected, thus providing opportunities to identify areas of low electrochemical activity, cracks, pinholes and water formation in fuel cell systems; while batteries can be examined for localised current generation and gas formation. Additionally, through the use of advanced thermal imaging techniques, bulk thermal properties can be identified, which can aid model development.

The use of thermal imaging in a correlative manner has also been examined in this article. It is this area which provides the greatest opportunity to understand the systems under examination in a truly holistic manner. By incorporating complementary techniques such as Raman spectroscopy, FTIR and X-ray microtomography into experiments, active processes can be understood in significantly greater depth and indeed synchronous process can be decoupled. Synchrotron radiation has also been shown to be a useful tool to be used in conjunction with thermal imaging. *In-situ* and *in-operando* experiments have to-date revealed structural deformations in SOFCs and the process of Li-ion battery failure; however, there are significant opportunities to expand on this work. X-ray techniques such as XRD and μCT enable high resolution microstructural information to be obtained, which can be used to generate physical models of systems, while the use of thermal imaging provides the boundary conditions for these models once more enabling the development of detailed and validated computational mechanisms to describe the behaviour of systems at a previously unattainable level of detail.

Acknowledgments: The authors would like to acknowledge the EPSRC funding for supporting the work of Robinson and Brett (EP/J001007/1); Brett and Shearing (EP/M009394/1, EP/M014045/1, EP/M014371/1); and the STFC for supporting Shearing and Brett (ST/K00171X/1), Shearing also acknowledges the Royal Academy of Engineering for funding.

Author Contributions: James Robinson prepared and wrote the manuscript. Paul Shearing and Dan Brett provided useful assistance in compiling and writing the manuscript.

Conflicts of Interest: The authors declare no conflict of interest.

References

1. Chan, S.H.; Khor, K.A.; Xia, Z.T. A complete polarization model of a solid oxide fuel cell and its sensitivity to the change of cell component thickness. *J. Power Sources* **2001**, *93*, 130–140. [CrossRef]
2. Huijsmans, J.P.P.; van Berkel, F.P.F.; Christie, G.M. Intermediate temperature SOFC—A promise for the 21st century. *J. Power Sources* **1998**, *71*, 107–110. [CrossRef]
3. Kharton, V.V.; Marques, F.M.B.; Atkinson, A. Transport properties of solid oxide electrolyte ceramics: A brief review. *Solid State Ion.* **2004**, *174*, 135–149. [CrossRef]
4. Spotnitz, R.; Franklin, J. Abuse behavior of high-power, lithium-ion cells. *J. Power Sources* **2003**, *113*, 81–100. [CrossRef]
5. Aiken, C.P.; Xia, J.; Wang, D.Y.; Stevens, D.A.; Trussler, S.; Dahn, J.R. An apparatus for the study of *in situ* gas evolution in Li-Ion pouch cells. *J. Electrochem. Soc.* **2014**, *161*, A1548–A1554. [CrossRef]
6. Hammami, A.; Raymond, N.; Armand, M. Lithium-ion batteries: Runaway risk of forming toxic compounds. *Nature* **2003**, *424*, 635–636. [CrossRef] [PubMed]
7. Wang, Q.; Sun, J.; Yao, X.; Chen, C. Thermal behavior of lithiated graphite with electrolyte in Lithium-Ion batteries. *J. Electrochem. Soc.* **2006**, *153*, A329–A333. [CrossRef]
8. Golubkov, A.W.; Fuchs, D.; Wagner, J.; Wiltsche, H.; Stangl, C.; Fauler, G.; Voitice, G.; Thalera, A.; Hackere, V. Thermal-runaway experiments on consumer Li-ion batteries with metal-oxide and olivin-type cathodes. *RSC Adv.* **2014**, *4*, 3633–3642. [CrossRef]
9. Tobishima, S.-I.; Yamaki, J.-I. A consideration of lithium cell safety. *J. Power Sources* **1999**, *81–82*, 882–886. [CrossRef]
10. Von Sacken, U.; Nodwell, E.; Sundher, A.; Dahn, J.R. Comparative thermal stability of carbon intercalation anodes and lithium metal anodes for rechargeable lithium batteries. *J. Power Sources* **1995**, *54*, 240–245. [CrossRef]
11. Armand, M.; Tarascon, J.M. Building better batteries. *Nature* **2008**, *451*, 652–657. [CrossRef] [PubMed]
12. Lu, L.; Han, X.; Li, J.; Hua, J.; Ouyang, M. A review on the key issues for lithium-ion battery management in electric vehicles. *J. Power Sources* **2013**, *226*, 272–288. [CrossRef]
13. Scrosati, B.; Hassoun, J.; Sun, Y.-K. Lithium-ion batteries. A look into the future. *Energy Environ. Sci.* **2011**, *4*, 3287–3295. [CrossRef]
14. National Transportation Safety Board. *Interim Factual Report*; DCA13IA037; National Transportation Safety Board: Boston, MA, USA, 7 January 2013.
15. Beauregard, G.P. Report of investigation: Hybrids plus plug in hybrid electric vehicle. Available online: http://priustouringclub.net/librairie/mediatheque/pdf/toyota-prius-a123-car-fire-investigation-report-2008.pdf (accessed on 1 October 2015).
16. Bandhauer, T.M.; Garimella, S.; Fuller, T.F. A critical review of thermal issues in Lithium-ion batteries. *J. Electrochem. Soc.* **2011**, *158*, R1–R25. [CrossRef]
17. Bazinski, S.J.; Wang, X. The influence of cell temperature on the entropic coefficient of a Lithium Iron Phosphate (LFP) pouch cell. *J. Electrochem. Soc.* **2014**, *161*, A168–A175. [CrossRef]
18. Srinivasan, V.; Wang, C.Y. Analysis of electrochemical and thermal behavior of Li-ion cells. *J. Electrochem. Soc.* **2003**, *150*, A98–A106. [CrossRef]
19. Li, Z.; Zhang, J.; Wu, B.; Huang, J.; Nie, Z.; Sun, Y.; An, F.Q.; Wu, N.N. Examining temporal and spatial variations of internal temperature in large-format laminated battery with embedded thermocouples. *J. Power Sources* **2013**, *241*, 536–553. [CrossRef]
20. Forgez, C.; Do, D.V.; Friedrich, G.; Morcrette, M.; Delacourt, C. Thermal modeling of a cylindrical LiFePO4/graphite lithium-ion battery. *J. Power Sources* **2010**, *195*, 2961–2968.
21. Richardson, R.R.; Ireland, P.T.; Howey, D.A. Battery internal temperature estimation by combined impedance and surface temperature measurement. *J. Power Sources* **2014**, *265*, 254–261. [CrossRef]

22. Schmidt, J.P.; Arnold, S.; Loges, A.; Werner, D.; Wetzel, T.; Ivers-Tiffée, E. Measurement of the internal cell temperature via impedance: Evaluation and application of a new method. *J. Power Sources* **2013**, *243*, 110–117. [CrossRef]
23. Nieto, N.; Díaz, L.; Gastelurrutia, J.; Blanco, F.; Ramos, J.C.; Rivas, A. Novel thermal management system design methodology for power lithium-ion battery. *J. Power Sources* **2014**, *272*, 291–302. [CrossRef]
24. Mills, A.; Al-Hallaj, S. Simulation of passive thermal management system for lithium-ion battery packs. *J. Power Sources* **2005**, *141*, 307–315. [CrossRef]
25. Li, Q.; Jensen, J.O.; Savinell, R.F.; Bjerrum, N.J. High temperature proton exchange membranes based on polybenzimidazoles for fuel cells. *Prog. Polym. Sci.* **2009**, *34*, 449–477. [CrossRef]
26. Chen, Z.; Higgins, D.; Yu, A.; Zhang, L.; Zhang, J. A review on non-precious metal electrocatalysts for PEM fuel cells. *Energy Environ. Sci.* **2011**, *4*, 3167–3192. [CrossRef]
27. Hawkes, A.D.; Brett, D.J.L.; Brandon, N.P. Fuel cell micro-CHP techno-economics: Part 1 – Model concept and formulation. *Int. J. Hydrog. Energy* **2009**, *34*, 9545–9557. [CrossRef]
28. Murray, E.P.; Tsai, T.; Barnett, S.A. A direct-methane fuel cell with a ceria-based anode. *Nature* **1999**, *400*, 649–651. [CrossRef] [PubMed]
29. O'Hayre, R.; Cha, S.-W.; Colella, W.; Prinz, F.B. *Fuel Cell Fundamentals*, 2nd ed.; John Wiley & Sons, Inc.: New York, NY, USA.
30. Apfel, H.; Rzepka, M.; Tu, H.; Stimming, U. Thermal start-up behaviour and thermal management of SOFC's. *J. Power Sources* **2006**, *154*, 370–378. [CrossRef]
31. Clague, R.; Marquis, A.J.; Brandon, N.P. Finite element and analytical stress analysis of a solid oxide fuel cell. *J. Power Sources* **2012**, *210*, 224–232. [CrossRef]
32. Lin, C.K.; Chen, T.T.; Chyou, Y.P.; Chiang, L.K. Thermal stress analysis of a planar SOFC stack. *J. Power Sources* **2007**, *164*, 238–251. [CrossRef]
33. Nakajo, A.; Wuillemin, Z.; van Herle, J.; Favrat, D. Simulation of thermal stresses in anode-supported solid oxide fuel cell stacks. Part I: Probability of failure of the cells. *J. Power Sources* **2009**, *193*, 203–215. [CrossRef]
34. Severson, H.; Assadi, M. Analysis of residual and operational thermal stresses in a planar SOFC. *J. Fuel Cell Sci. Technol.* **2013**, *10*, 061001. [CrossRef]
35. Morel, B.; Roberge, R.; Savoie, S.; Napporn, T.W.; Meunier, M. Temperature and performance variations along single chamber solid oxide fuel cells. *J. Power Sources* **2009**, *186*, 89–95. [CrossRef]
36. Leone, P.; Lanzini, A.; Delhomme, B.; Ortigoza-Villalba, G.A.; Smeacetto, F.; Santarelli, M. Analysis of the thermal field of a seal-less planar solid oxide fuel cell. *J. Power Sources* **2012**, *204*, 100–105. [CrossRef]
37. Vollmer, M.; Mollmann, K.P. *Infrared Thermal Imaging*; Wiley-VCH: Weinheim, Germany, 2010.
38. Meola, C. *Infrared Thermography: Recent Advances and Future Trends*; Bentham Science Publishers: Emirate of Sharjah, United Arab Emirates, 2012.
39. Obeisun, O.A.; Meyer, Q.P.-G.; Robinson, J.; Gibbs, C.; Kucernak, A.R.J.; Shearing, P.R.; Brett, D.J.L. Advanced diagnostics applied to a self-breathing fuel cell. *ECS Trans.* **2014**, *61*, 249–258. [CrossRef]
40. Obeisun, O.A.; Meyer, Q.; Robinson, J.; Gibbs, C.W.; Kucernak, A.R.; Shearing, P.R.; Brett, D.J.L. Development of open-cathode polymer electrolyte fuel cells using printed circuit board flow-field plates: Flow geometry characterisation. *Int. J. Hydrog. Energy* **2014**, *39*, 18326–18336. [CrossRef]
41. Martins, L.S.; Gardolinski, J.E.F.C.; Vargas, J.V.C.; Ordonez, J.C.; Amico, S.C.; Forte, M.M.C. The experimental validation of a simplified PEMFC simulation model for design and optimization purposes. *Appl. Therm. Eng.* **2009**, *29*, 3036–3048. [CrossRef]
42. Matian, M.; Marquis, A.J.; Brandon, N.P. Application of thermal imaging to validate a heat transfer model for polymer electrolyte fuel cells. *Int. J. Hydrog. Energy* **2010**, *35*, 12308–12316. [CrossRef]
43. Dedigama, I.; Angeli, P.; Ayers, K.; Robinson, J.B.; Shearing, P.R.; Tsaoulidis, D.; Brett, D.J.L. *In situ* diagnostic techniques for characterisation of polymer electrolyte membrane water electrolysers—Flow visualisation and electrochemical impedance spectroscopy. *Int. J. Hydrog. Energy* **2014**, *39*, 4468–4482. [CrossRef]
44. Hakenjos, A.; Hebling, C. Spatially resolved measurement of PEM fuel cells. *J. Power Sources* **2005**, *145*, 307–311. [CrossRef]
45. Shimoi, R.; Masuda, M.; Fushinobu, K.; Kozawa, Y.; Okazaki, K. Visualization of the membrane temperature field of a polymer electrolyte fuel cell. *J. Energy Resour. Technol.* **2004**, *126*, 258–261. [CrossRef]

46. Guo, H.; Wang, M.H.; Liu, J.X.; Nie, Z.H.; Ye, F.; Ma, C.F. Temperature distribution on anodic surface of membrane electrode assembly in proton exchange membrane fuel cell with interdigitated flow bed. *J. Power Sources* **2015**, *273*, 775–783. [CrossRef]
47. Daino, M.M.; Lu, Z.; LaManna, J.M.; Owejan, J.P.; Trabold, T.A.; Kandlikar, S.G. Through-plane water transport visualization in a PEMFC by visible and infrared imaging. *Electrochem. Solid-State Lett.* **2011**, *14*, B51–B54. [CrossRef]
48. Kim, U.S.; Shin, C.B.; Kim, C.S. Modeling for the scale-up of a lithium-ion polymer battery. *J. Power Sources* **2009**, *189*, 841–846. [CrossRef]
49. Kim, U.S.; Shin, C.B.; Kim, C.S. Effect of electrode configuration on the thermal behavior of a lithium-polymer battery. *J. Power Sources* **2008**, *180*, 909–916. [CrossRef]
50. Wang, Z.J.; Li, Z.Q.; Liu, Q. Infrared thermography non-destructive evaluation of lithium-ion battery. *Proc. SPIE* **2011**, *8193*. [CrossRef]
51. Waldmann, T.; Bisle, G.; Hogg, B.-I.; Stumpp, S.; Danzer, M.A.; Kasper, M.; Axmann, P.; Wohlfahrt-Mehrens, M. Influence of Cell Design on Temperatures and Temperature Gradients in Lithium-Ion Cells: An In Operando Study. *J. Electrochem. Soc.* **2015**, *162*, A921–A927. [CrossRef]
52. Pesaran, A.A.; Vlahinos, A.; Burch, S.D. Thermal performance of EV and HEV battery modules and packs. National Renewable Energy Laboratory: Golden, CO, USA, 1997.
53. Keyser, M.A.; Pesaran, A.; Oweis, S.; Chagnon, G.; Ashtiani, C. *Thermal Evaluation and Performance of High-Power Lithium-Ion Cells*; National Renewable Energy Laboratory: Golden, CO, USA, 1999.
54. Bharathan, D.; Pesaran, A.; Vlahinos, A.; Kim, G.H. Improving battery design with electro-thermal modeling. In Proceedings of the 2005 IEEE Vehicle Power and Propulsion, Chicago, IL, USA, 7–9 September 2005.
55. Noorkami, M.; Robinson, J.B.; Meyer, Q.; Obeisun, O.; Fraga, E.S.; Reisch, T.; Shearing, P.R.; Brett, D.J.L. Effect of temperature uncertainty on polymer electrolyte fuel cell performance. *Int. J. Hydrog. Energy* **2014**, *39*, 1439–1448. [CrossRef]
56. Meyer, Q.; Ashton, S.; Curnick, O.; Reisch, T.P.A.; Ronaszegi, K.; Robinson, J.B.; Brett, D.J.L. Dead-ended anode polymer electrolyte fuel cell stack operation investigated using electrochemical impedance spectroscopy, off-gas analysis and thermal imaging. *J. Power Sources* **2014**, *254*, 1–9. [CrossRef]
57. Robinson, J.B.; Engebretsen, E.; Finegan, D.P.; Darr, J.; Hinds, G.; Shearing, P.R.; Brett, D.J.L. Detection of Internal Defects in Lithium-Ion Batteries Using Lock-in Thermography. *ECS Electrochem. Lett.* **2015**, *4*, A106–A109. [CrossRef]
58. Engebretsen, E.; Robinson, J.B.; Obeisun, O.; Mason, T.; Finegan, D.P.; Hinds, G.; Shearing, P.R.; Brett, D.J.L. Electro-thermal impedance spectroscopy applied to an open-cathode polymer electrolyte fuel cell. *J. Power Sources* **2016**, *302*, 210–214. [CrossRef]
59. Pomfret, M.B.; Steinhurst, D.A.; Owrutsky, J.C. Methanol and Ethanol Fuels in Solid Oxide Fuel Cells: A Thermal Imaging Study of Carbon Deposition. *Energy Fuels* **2011**, *25*, 2633–2642. [CrossRef]
60. Pomfret, M.B.; Steinhurst, D.A.; Kidwell, D.A.; Owrutsky, J.C. Thermal imaging of solid oxide fuel cell anode processes. *J. Power Sources* **2010**, *195*, 257–262. [CrossRef]
61. Pomfret, M.B.; Steinhurst, D.A.; Owrutsky, J.C. Ni/YSZ solid oxide fuel cell anodes operating on humidified ethanol fuel feeds: An optical study. *J. Power Sources* **2013**, *233*, 331–340. [CrossRef]
62. Pomfret, M.B.; Steinhurst, D.A.; Owrutsky, J.C. Thermal Imaging of Solid Oxide Fuel Cell Anode Degradation with Dry and Wet Ethanol Fuel Flows. *ECS Trans.* **2011**, *35*, 1563–1570.
63. Pomfret, M.B.; Steinhurst, D.A.; Owrutsky, J.C. Methanol as an Oxygenated SOFC Fuel: An In Situ Optical Analysis of the Fuel Utilization Chemical Mechanism. *ECS Trans.* **2013**, *57*, 2903–2912. [CrossRef]
64. Brett, D.J.L.; Aguiar, P.; Clague, R.; Marquis, A.J.; Schöttl, S.; Simpson, R.; Brandon, N.P. Application of infrared thermal imaging to the study of pellet solid oxide fuel cells. *J. Power Sources* **2007**, *166*, 112–119. [CrossRef]
65. Schöttl, S.; Brett, D.J.L. *Applications of Thermal Imaging in Solid Oxide Fuel Cell Research*; NPL Report DEPC-TH 007; National Physical Laboratory: London, UK, 2006.
66. Cumming, D.J.; Elder, R.H. Thermal imaging of solid oxide cells operating under electrolysis conditions. *J. Power Sources* **2015**, *280*, 387–392. [CrossRef]
67. Cumming, D.J.; Taylor, R.; Manerova, J.; Sinclair, D.C.; Hardacre, C.; Elder, R.H. In-Situ Monitoring of Solid Oxide Electrolysis Cells. *ECS Trans.* **2013**, *58*, 207–216. [CrossRef]

68. Hunt, I.A.; Patel, Y.; Szczygielski, M.; Kabacik, L.; Offer, G.J. Lithium sulfur battery nail penetration test under load. *J. Energy Storage* **2015**, *2*, 25–29. [CrossRef]
69. Hatchard, T.D.; Trussler, S.; Dahn, J.R. Building a "smart nail" for penetration tests on Li-ion cells. *J. Power Sources* **2014**, *247*, 821–823. [CrossRef]
70. Doh, C.-H.; Kim, D.-H.; Kim, H.-S.; Shin, H.-M.; Jeong, Y.-D.; Moon, S.-I.; Jin, B.-S.; Eom, S.W.; Kim, H.-S.; Kim, K.W.; *et al*. Thermal and electrochemical behaviour of C/LixCoO2 cell during safety test. *J. Power Sources* **2008**, *175*, 881–885. [CrossRef]
71. Kim, U.S.; Yi, J.; Shin, C.B.; Han, T.; Park, S. Modeling the Thermal Behaviors of a Lithium-Ion Battery during Constant-Power Discharge and Charge Operations. *J. Electrochem. Soc.* **2013**, *160*, A990–A995. [CrossRef]
72. Yi, J.; Kim, U.S.; Shin, C.B.; Han, T.; Park, S. Three-Dimensional Thermal Modeling of a Lithium-Ion Battery Considering the Combined Effects of the Electrical and Thermal Contact Resistances between Current Collecting Tab and Lead Wire. *J. Electrochem. Soc.* **2013**, *160*, A437–A443. [CrossRef]
73. Duan, J.; Wei, B.; Yang, R.; Cai, C.; Pan, J. Screening defective lithium ion batteries of 0 V open-circuit voltage by a high current charge process in combination with *in situ* infrared thermal imaging technology. *J. Solid State Electrochem.* **2012**, *16*, 597–602. [CrossRef]
74. Robinson, J.B.; Darr, J.A.; Eastwood, D.S.; Hinds, G.; Lee, P.D.; Shearing, P.R.; Taiwo, O.O.; Brett, D.J.L. Non-uniform temperature distribution in Li-ion batteries during discharge–A combined thermal imaging, X-ray micro-tomography and electrochemical impedance approach. *J. Power Sources* **2014**, *252*, 51–57. [CrossRef]
75. Finegan, D.P.; Scheel, M.; Robinson, J.B.; Tjaden, B.; Hunt, I.; Mason, T.J.; Millichamp, J.; Di Michiel, M.; Offer, G.J.; Hinds, G.; *et al*. In-operando high-speed tomography of lithium-ion batteries during thermal runaway. *Nat. Commun.* **2015**, *6*. [CrossRef] [PubMed]
76. Robinson, J.B.; Brown, L.D.; Jervis, R.; Taiwo, O.O.; Heenan, T.M.M.; Millichamp, J.; Mason, T.J.; Neville, T.P.; Clague, R.; Eastwood, D.S.; *et al*. Investigating the effect of thermal gradients on stress in solid oxide fuel cell anodes using combined synchrotron radiation and thermal imaging. *J. Power Sources* **2015**, *288*, 473–481. [CrossRef]
77. Robinson, J.B.; Brown, L.D.; Jervis, R.; Taiwo, O.O.; Millichamp, J.; Mason, T.J.; Neville, T.P.; Eastwood, D.S.; Reinhard, C.; Lee, P.D.; *et al*. A novel high-temperature furnace for combined *in situ* synchrotron X-ray diffraction and infrared thermal imaging to investigate the effects of thermal gradients upon the structure of ceramic materials. *J. Synchrotron Radiat.* **2014**, *21*, 1134–1139. [CrossRef] [PubMed]
78. Robinson, J.B.; Engebretsen, E.; Brown, L.D.; Clague, R.; Eastwood, D.; Reinhard, C.; Lee, P.; Brett, D.J.L.; Shearing, P.R. Thermal Gradients in Solid Oxide Fuel Cell Anodes: X-Ray Diffraction, Thermal Imaging and Model Prediction. *ECS Trans.* **2015**, *68*, 1053–1067. [CrossRef]
79. Kirtley, J.D.; Steinhurst, D.A.; Owrutsky, J.C.; Pomfret, M.B.; Walker, R.A. In situ optical studies of methane and simulated biogas oxidation on high temperature solid oxide fuel cell anodes. *Phys. Chem. Chem. Phys.* **2014**, *16*, 227–236. [CrossRef] [PubMed]
80. Eigenbrodt, B.C.; Pomfret, M.B.; Steinhurst, D.A.; Owrutsky, J.C.; Walker, R.A. Direct, *In Situ* Optical Studies of Ni−YSZ Anodes in Solid Oxide Fuel Cells Operating with Methanol and Methane. *J. Phys. Chem. C* **2011**, *115*, 2895–2903. [CrossRef]

© 2016 by the authors; licensee MDPI, Basel, Switzerland. This article is an open access article distributed under the terms and conditions of the Creative Commons by Attribution (CC-BY) license (http://creativecommons.org/licenses/by/4.0/).